CFA-1: the first chiral metal–organic framework containing Kuratowski-type secondary building units†

Phillip Schmieder,[a] Dmytro Denysenko,[a] Maciej Grzywa,[a] Benjamin Baumgärtner,[a] Irena Senkovska,[b] Stefan Kaskel,[b] German Sastre,[c] Leo van Wüllen[d] and Dirk Volkmer*[a]

The novel homochiral metal–organic framework CFA-1 (Coordination Framework Augsburg-1), $[Zn_5(OAc)_4(bibta)_3]$, containing the achiral linker {H_2-bibta = 1*H*,1′*H*-5,5′-bibenzo[*d*][1,2,3]triazole}, has been synthesised. The reaction of H_2-bibta and $Zn(OAc)_2{\cdot}2H_2O$ in *N*-methylformamide (NMF) (90 °C, 3 d) yields CFA-1 as trigonal prismatic single crystals. CFA-1 serves as a convenient precursor for the synthesis of isostructural frameworks with redox-active metal centres, which is demonstrated by the postsynthetic exchange of Zn^{2+} by Co^{2+} ions. The framework is robust to solvent removal and has been structurally characterized by synchrotron single-crystal X-ray diffraction and solid state NMR measurements (^{13}C MAS- and ^{1}H MAS-NMR at 10 kHz). Results from MAS-NMR and IR spectroscopy studies are corroborated by cluster and periodic DFT calculations performed on CFA-1 cluster fragments.

Introduction

Research on metal–organic frameworks (MOFs) has matured into a well-established field of solid state science, ever since the first seminal publications appeared in the literature.[1] MOFs can be applied as materials for gas storage or separation, catalysis and magnetic or optical applications, as has been proposed in several review articles.[2]

Chiral metal–organic frameworks, in particular, are interesting for the purpose of enantioselective separation or catalysis. There are currently three different strategies to synthesise chiral MOFs. The first approach relies on the usage of enantiomerically pure, chiral organic linkers, the absolute configuration of which is retained during framework self-assembly. Among the first examples of catalytically active MOFs, Kim *et al.* have reported on a zinc based homochiral network employing a chiral ligand derived from tartaric acid.[3] MOFs containing chiral binaphthyl linkers were published by the group of Lin.[4] Utilisation of enantiomerically pure ligands to build up homochiral networks is a broadly applicable approach if the ligand preparation is feasible within a few steps and no racemisation occurs during framework synthesis. A second alternative route is to prepare MOFs from achiral ligands and (inexpensive) chiral auxiliary templates. Rosseinsky *et al.*, for instance, made use of enantiomerically pure 1,2-propanediol as a chiral co-ligand.[5] The 1,2-propanediol coordinates to the metal center, allowing to control the absolute helicity of the growing polymeric structure and to determine the nature of interpenetration. The third approach for obtaining homochiral MOFs is based on the spontaneous self-resolution of chiral frameworks. As an example, Aoyama *et al.* reported on a chiral MOF $Cd(apd)(NO_3)_2{\cdot}H_2O{\cdot}EtOH$ with Cd^{2+} ions and 5-(9-anthracenyl)pyrimidine (*apd*) serving as bridging ligands.[6] The metal ion is six-fold coordinated including two pyrimidine ligands in which the chirality arises from a twist of the coordinating pyrimidine rings.[7]

Employing the approach of self-resolution we here report on the synthesis and the structure of a novel chiral MOF CFA-1 (**2**) which forms from the achiral linker $bibta^{2-}$ (H_2-bibta = 1*H*,1′*H*-5,5′-bibenzo[*d*][1,2,3]triazole (**1**)) (Scheme 1).

A synchrotron single X-ray diffraction study revealed a composition of the framework of CFA-1 which is formulated as $[Zn_5(OAc)_4(bibta)_3]$, crystallizing in the chiral space group *P*321 (no. 150). CFA-1 represents the first example of chiral coordination frameworks containing the Kuratowski-type[8] SBU, a structurally robust pentanuclear coordination unit of the

[a]*Institute of Physics, Chair of Solid State and Materials Science, Augsburg University, Universitaetsstrasse 1, 86159 Augsburg, Germany.*
E-mail: dirk.volkmer@physik.uni-augsburg.de; Fax: +49 (0)821 598 5955; Tel: +49 (0)821 598 3006
[b]*Department of Inorganic Chemistry, Dresden University of Technology, Bergstrasse 66, 01062 Dresden, Germany*
[c]*Instituto de Tecnologia Quimica CSIC-UPV, Universidad Politecnica de Valencia, Av. Los Naranjos s/n, 46022 Valencia, Spain*
[d]*Institute of Physics, Chair of Chemical Physics and Materials Science, Augsburg University, Universitaetsstrasse 1, 86159 Augsburg, Germany*
†Electronic supplementary information (ESI) available: Spectral data, details of NMR measurements and computational studies. CCDC 930634 and 930635. For ESI and crystallographic data in CIF or other electronic format see DOI: 10.1039/c3dt50787d

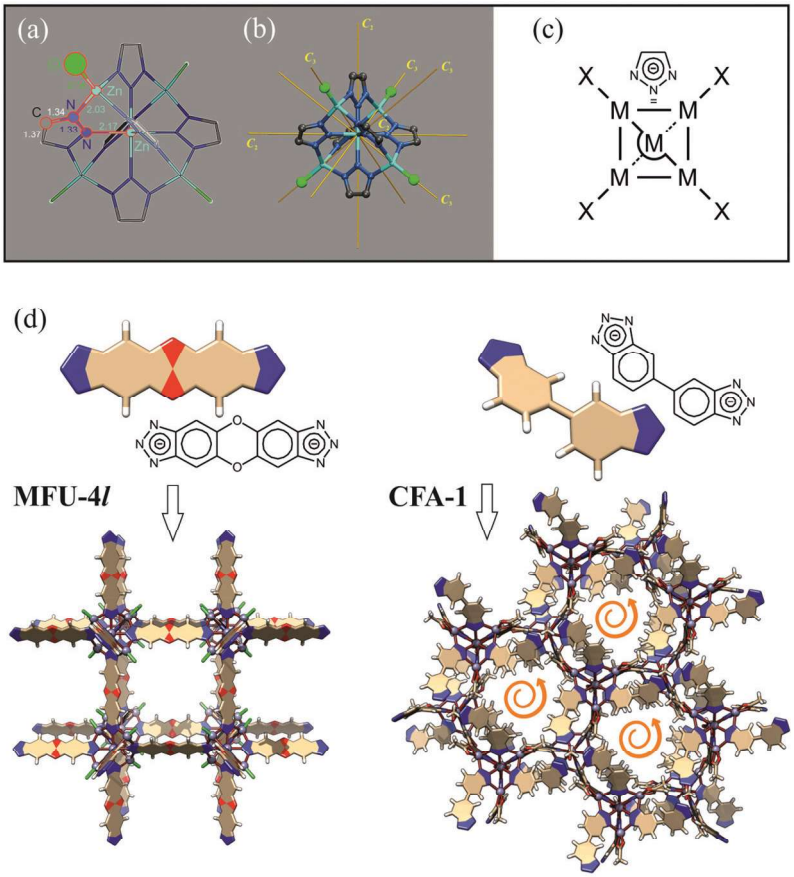

Scheme 1 (a) Kuratowski-type metal complex $[Zn_5Cl_4(ta)_6]$, red marked fragments indicating typical bond lengths of the coordination unit;[8b] (b) symmetry elements of the Kuratowski unit (T_d point group symmetry); and (c) its corresponding skeletal representation;[8d] (d) frameworks containing Kuratowski-type secondary building units.

general formula $[M^{II}{}_5X_4(L)_6]$, which forms spontaneously for a huge variety of (divalent) metal salts ($M^{II}X_2$) and triazolate ligands (L) (Scheme 1) (X = Cl^-, Br^-, I^-, NO_3^-, OH^-, acetate or acetylacetonate).[8,9]

The first MOFs containing Kuratowski-type secondary building units, MFU-4 and MFU-4*l*,[8d,10] were built from linear bis-triazolate linkers which led to the formation of highly symmetric, cubic framework structures (Scheme 1(d), left). The framework CFA-1 described in the following, in contrast, is built up from a skewed bis-triazolate ligand featuring a biphenyl-type backbone, which introduces dissymmetry into the MOF, thus leading to helical channels that run along the *c*-direction of the trigonal crystal lattice (Scheme 1(d), right). Crystalline precipitates of CFA-1 accordingly contain two different enantiomorphous crystal forms, which are obtained at equal ratio.

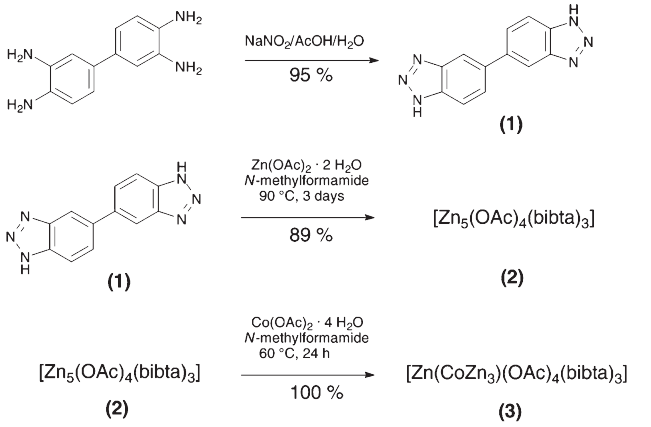

Scheme 2 Synthesis of H_2-bibta (**1**); synthesis of metal–organic framework (**2**) and synthesis of hetero-metallic framework (**3**).

Results and discussion

Syntheses and characterisation

The achiral H_2-bibta ligand was synthesised in one step from commercially available 3,3′,4,4′-tetraaminobiphenyl (Scheme 2). Light brown trigonal prisms of CFA-1 were obtained from zinc acetate dihydrate and H_2-bibta in *N*-methylformamide at 90 °C (Scheme 2).

Crystal structure analysis

A synchrotron single X-ray diffraction study reveals that CFA-1 crystallises in the trigonal crystal system in the chiral space

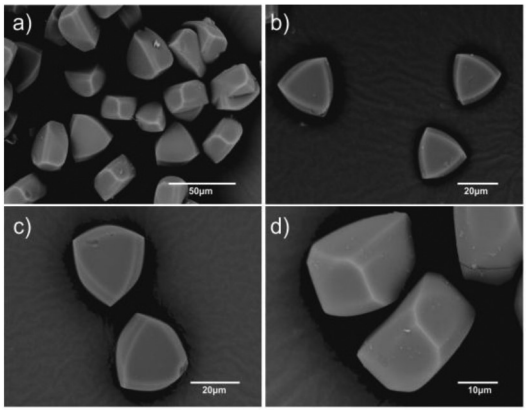

Fig. 1 SEM micrographs of CFA-1; (a) a low magnification image; (b) to (d) typical shape of the trigonal prismatic enantiomorphous crystals as viewed along the *c*-axis (b, c), as viewed along the <110> direction (d).

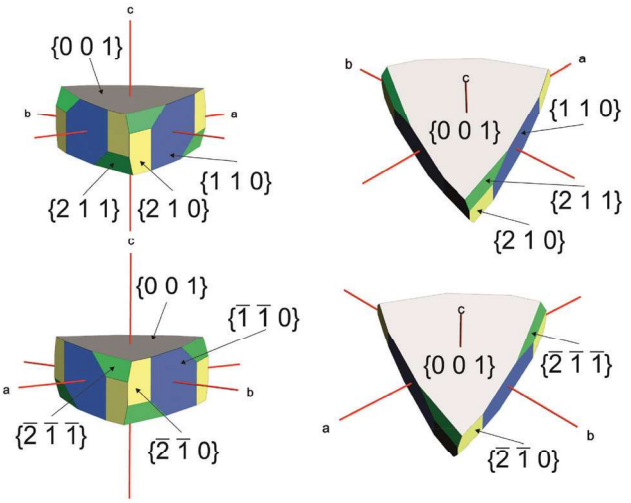

Fig. 2 Simulated morphology of the two enantiomorphous forms of CFA-1 crystals (**2**). Miller indices of symmetry equivalent crystal faces are given in brackets. (Simulated with WinXMorph.[11])

group *P*321 (no. 150). The crystalline sample of the metal–organic framework is a racemic mixture of two enantiomorphous forms of CFA-1 crystals. It is thus not possible to bring the two existing mirror-symmetric crystal forms into congruence (Fig. 1 and 2). The asymmetric unit consists of three zinc, sixteen carbon, six nitrogen, six oxygen and sixteen hydrogen atoms. An Ortep-style plot of the asymmetric unit with atom labels is shown in Fig. 3.

CFA-1 is constructed from $\{Zn_5(OAc)_4\}^{6+}$ secondary building units interconnected by achiral bibta^{2-} linkers. The central Zn^{2+} ion (Zn1), placed at a site of 3 symmetry, is octahedrally coordinated (Fig. 4). The four peripheral Zn^{2+} ions (Zn2 and three times Zn3, positioned at sites of 3 and 1 symmetry, respectively), are five-fold-coordinated. The different local coordination environments of Zn2 and Zn3 are shown in Fig. 5.

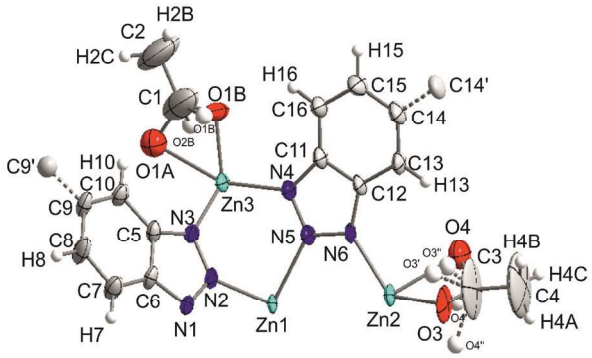

Fig. 3 Ortep-style diagram of the asymmetric unit of CFA-1 (**2**) (atoms displayed as 50% probability ellipsoids). (Disordered and symmetry-generated oxygen atoms indicated by white globes.)

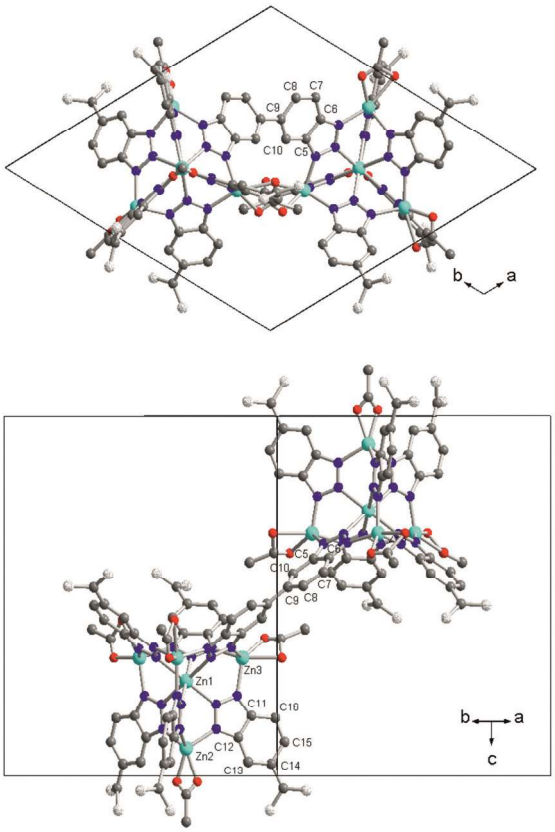

Fig. 4 Crystal packing diagrams of CFA-1. Top: ball-and-stick representation of two Kuratowksi-type SBUs (as viewed along the *c*-axis); bottom: the same fragment (as viewed along the [110] direction). (Some C atoms belonging to bibta^{2-} linkers are shown as white globes in order to indicate the position of the appended benzene moieties.)

Each $\{Zn_5\}$ unit is connected to six bibta^{2-} ligands by 18 Zn–N bonds, with each ligand coordinating to one central and two peripheral Zn ions. The zinc–nitrogen bond distances span a range of 2.191(3)–2.203(3) Å for the octahedrally coordinated Zn1 and 2.037(3)–2.043(3) Å for Zn2 and Zn3. These values are in good agreement with those found in structurally related Zn triazolate compounds.[8,10] Two different positions of

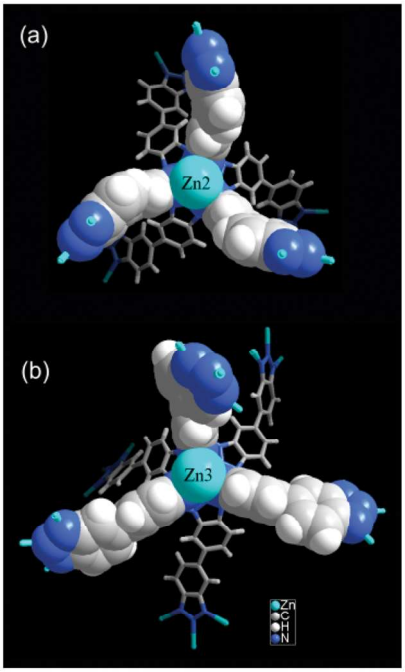

Fig. 5 Coordination environments of Zn2 and Zn3 in the Kuratowski-type secondary building units of CFA-1 (**2**). (Acetate ligands are omitted for clarity. Benzotriazolate ligands which bind to the labeled zinc atoms are drawn as CPK models.)

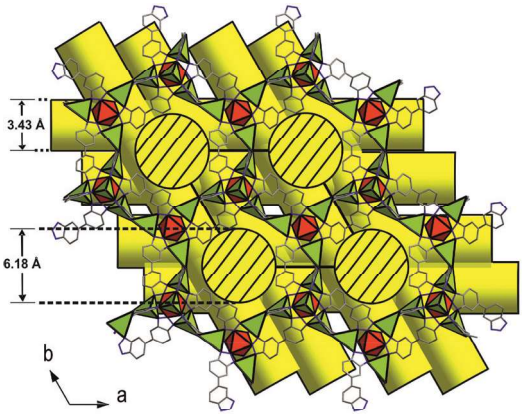

Fig. 6 Schematic representation showing the open channels in the crystal structure of CFA-1 (view along the *c*-direction).

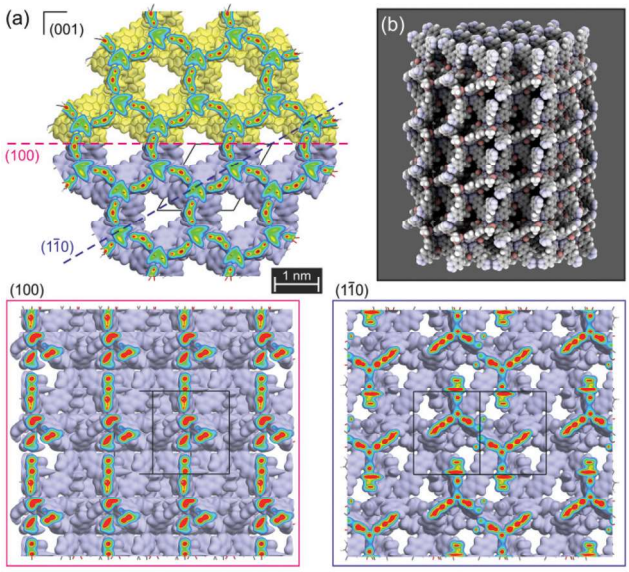

Fig. 7 Packing models of CFA-1. (a) Top: channels running along the *c*-direction of the trigonal crystal system. Framework atoms are represented by colour-coded electron density isosurfaces (light yellow/blue = 0.1 e^{-} $Å^{-1}$).[14] Bottom: view onto different cuts through the framework as defined by the intercepted lines running through (001), representing the traces of the crystal planes ||(100) and ||(1$\bar{1}$0). (b) 3-d perspective space-filling model of CFA-1.[15]

distorted acetate ligands are observed in the structure of CFA-1. One of these, coordinated to the Zn2 ion, is placed on an axis of 3-fold symmetry leading to a threefold positional disorder around this axis. The second acetate ligand, coordinating to the Zn3 atom, shows a two-fold disorder (nearly equal probabilities) which has no relation to crystallographic symmetry. The two benzotriazolate moieties of the $bibta^{2-}$ ligand are twisted with respect to each other. The two least-squares planes running through atoms assigned as {N1–N3, C5–C10} and {N4–N6, C11–C16}, enclose angles of 42.1(2)° and 36.4(2)°, respectively. CFA-1 features a 3-D microporous structure constructed from Kuratowski-type SBUs. The packing diagram of CFA-1, depicted in Fig. 6 and 7, shows 3-D interconnected hydrophobic channels running along the *a*- and *c*-directions of the crystal lattice. The trigonal prismatic voids with a maximal width of 14.35 Å (the closest distance between C-atoms of phenyl rings, taking into account van der Waals radii of C-atoms (1.7 Å)) are connected to each other through two different types of windows: narrow ones extending in the [100] and [010] directions with a diameter of 3.43 Å (the distance between C-atoms of CH_3-groups, taking into account van der Waals radii of C-atoms (1.7 Å)) and wide ones running in the [001] direction with a diameter of 6.18 Å (the distance between H-atoms of phenyl rings, taking into account van der Waals radii of H-atoms (1.2 Å)). The channels are occupied by disordered solvent molecules the positions of which were impossible to resolve and refine from electron density distribution. The SQUEEZE procedure[12] gives an electron count of 615 per unit cell which corresponds to about 19 *N*-methylformamide (NMF) molecules in the unit cell of CFA-1. The calculation of solvent content using single crystal analysis suggests $[Zn_5(OAc)_4(bibta)_3]\cdot 9.5NMF$ for the composition of CFA-1. A calculation with PLATON/SQUEEZE[12] reveals that the initial solvent accessible void volume of CFA-1 is 3163.2 $Å^3$ (0.753 cm^3 g^{-1}), which is 60.4% of the unit cell volume (5236.6 $Å^3$) for a probe radius of 1.68 Å, corresponding to the approximate van der Waals radius of Ar.[13] An estimation with the program PLATON/SQUEEZE[12] for NMF molecules with an approximate van der Waals radius of 2.58 Å reveals that the initial solvent accessible void volume is 2577.3 $Å^3$ (0.613 cm^3 g^{-1}), which is 49.2% of the unit cell volume (5236.6 $Å^3$). Assuming that the density of NMF in the pores is equal to the

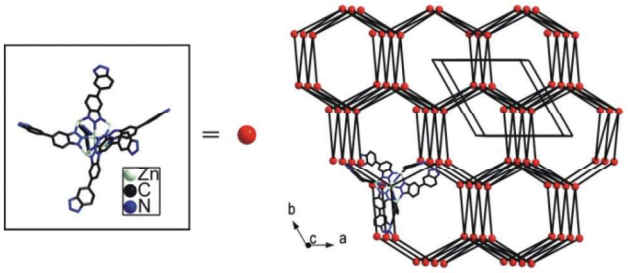

Fig. 8 Topological representation of **CFA-1** showing the **acs**-type net. Distorted acetate groups are omitted for clarity.

density of bulk NMF (1.00 g cm^{-3}), the unit cell must contain 23 NMF molecules (or 38 wt%), which is slightly higher than the solvent content suggested by crystallographic data.

The CFA-1 coordination network can be schematized by representing Kuratowski-type SBUs as 6-connected nodes and the bibta-ligands as spacer of length 13.67(2)–14.42(2) Å. The network topology type is **acs** (see Fig. 8).[16]

Selected bond lengths for CFA-1 are presented in Table 1. The atomic coordinates and isotropic thermal parameters and the list of bond distances and angles are presented in Tables S1–S3.†

Thermal analysis and VTXRPD studies

Thermal and structural stability of CFA-1 (**2**) and Co–CFA-1 (**3**) was confirmed by TGA and VTXRPD measurements. In the TGA curves of **2** and **3** (Fig. 9) the gradual weight loss of about 45% in the range of 25–300 °C is attributed to the removal of all solvent molecules (calc. 38%). Prior to measurement, both samples were treated several times with fresh *N*-methylformamide and stored over fresh NMF in order to saturate the pores with solvent molecules. However, the solvent content is higher than calculated using the crystal structure data, indicating that presumably a considerable amount of solvent is adsorbed on the external surface or within intercrystalline voids.

The experimental XRPD pattern is consistent with the simulated XRPD from the single-crystal X-ray diffraction data

Table 1 Selected bond lengths of CFA-1

Atoms	Bond lengths (Å)
Zn(1)–N(5)	2.191(3)
Zn(1)–N(2)	2.203(3)
Zn(2)–O(4)	1.936(10)
Zn(2)–N(6)	2.038(3)
Zn(2)–O(3)	2.345(11)
Zn(2)–C(3)	2.493(15)
Zn(3)–O(2A)	1.943(6)
Zn(3)–O(1B)	2.013(6)
Zn(3)–N(4)	2.037(3)
Zn(3)–N(3)	2.038(3)
Zn(3)–N(1)#1	2.043(3)
Zn(3)–O(2B)	2.259(7)
Zn(3)–O(1A)	2.339(7)
Zn(3)–C(1)	2.455(6)

Symmetry transformations used to generate equivalent atoms: #1 $-x + y$, $-x + 1$, z; #2 $-y + 1$, $x - y + 1$, z.

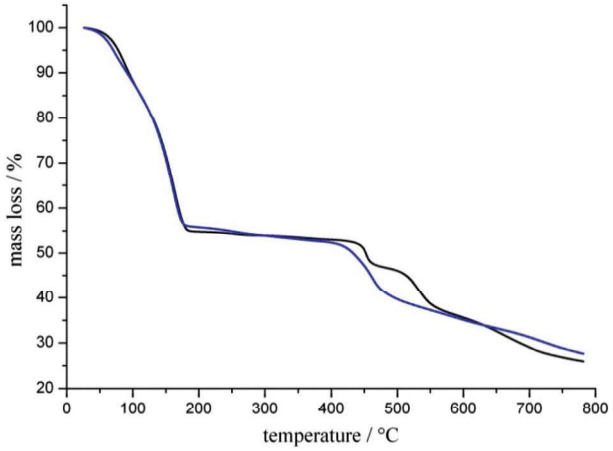

Fig. 9 Thermogravimetric analysis of **2** (black curve) and **3** (blue graph) under a nitrogen atmosphere.

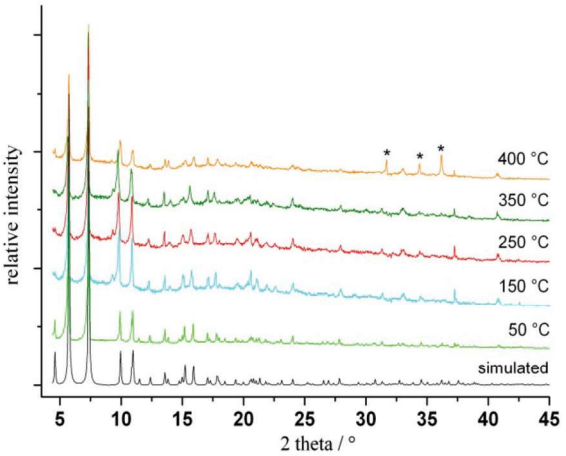

Fig. 10 VTXRPD patterns of **2** in the range of 50–400 °C. The first XRPD pattern is simulated from the single crystal structure of **2** (*peaks belong to ZnO).

(Fig. 10). Variable temperature X-ray powder diffraction studies of **2** (Fig. 10) and **3** (Fig. 11) show that both frameworks are stable up to 350 °C and crystallinity is retained upon loss of *N*-methylformamide molecules. At 400 °C, zinc oxide (PDF no. 36-1451) appears as a new crystal phase (Fig. 10).

The decomposition of the frameworks starts between 350 and 400 °C (Fig. 9), which is in good agreement with VTXRPD data (Fig. 10 and 11).

Moreover, it is possible to obtain a heterometallic derivative of **2** by postsynthetic metal exchange, as described previously for MFU-4*l*.[17] Heating up **2** with a solution of $Co(OAc)_2 \cdot 4H_2O$ in NMF leads to replacement of Zn^{2+} by Co^{2+} ions (Scheme 2). As proved by elemental analysis for compound **3** and Ar sorption isotherms, the modified framework does not contain residual cobalt acetate, since the pore volume does not change after metal exchange (Fig. 16). Depending on the Co/Zn molar ratio of the initial suspension, different numbers of zinc centres can be replaced by Co^{2+} ions (Fig. 12). Similarly to

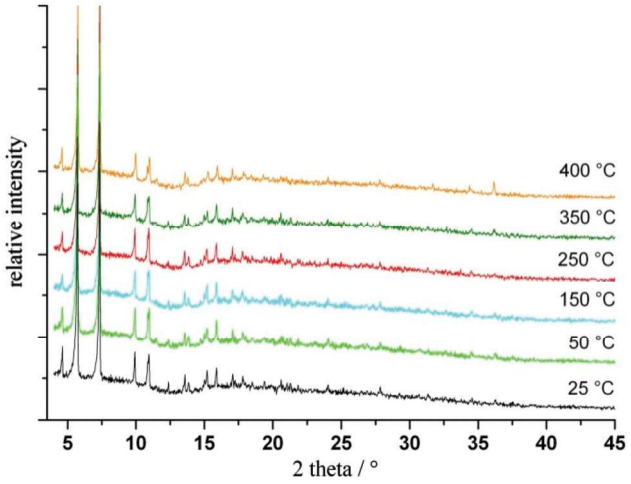

Fig. 11 VTXRPD plots of **3** in the range of 25–400 °C.

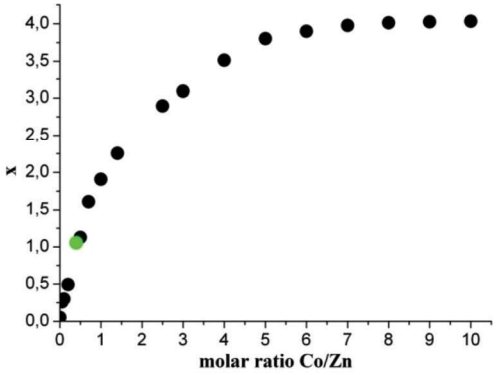

Fig. 12 Total number *x* of Co^{2+} ions per $\{Co_xZn_{5-x}(OAc)_4\}^{6+}$ unit as a function of the (Co/Zn) molar ratio after metal ion exchange reaction in NMF at 60 °C, determined by energy-dispersive X-ray spectroscopy (EDX). The green marked data point corresponds to the experimental conditions applied in the synthesis of Co–CFA-1 (**3**).

MFU-4*l*, the exchange curve shows that only 4 of the 5 Zn centres in each $\{Zn_5(OAc)_4\}^{6+}$ unit can be exchanged, indicating that octahedrally coordinated zinc centres cannot be replaced under the applied experimental conditions. The complete exchange of all four peripheral zinc ions requires a huge excess of cobalt ions in solution. These cobalt-containing frameworks are of potential interest for catalytic applications. Adjusting a (Co/Zn) molar ratio of 0.40 in the ion exchange experiment for instance (see Fig. 12, green marked data point), a novel CFA-1 derivative termed Co–CFA-1 (**3**) is obtained, in which on average one Zn^{2+} is replaced by a Co^{2+} ion per Kuratowski unit.

UV-vis-NIR spectroscopy

The diffuse reflectance UV-vis-NIR spectrum of **3** displays five absorption bands at 567, 741, 1027, 1413 and 1708 nm (Fig. 13). To obtain the positions of the last four absorption bands, a component analysis of the spectrum was performed employing Gauss-type fit functions of Origin 8.5 program.[18]

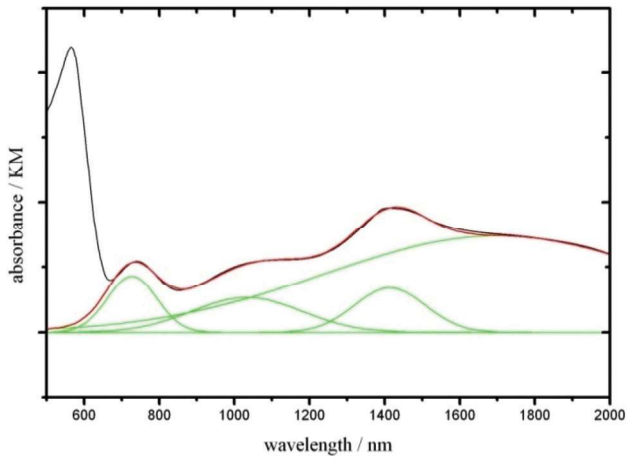

Fig. 13 Solid-state UV-vis-NIR spectrum of Co–CFA-1 (**3**) (black curve); fitted Gauss-functions (green curves) and the resulting graph of four different Gauss fits (red curve).

The positions of the band maximums are in good agreement with typical spectra of five-fold coordinated Co^{2+} complexes as described in the literature.[19] Thus, the $Co(NP_3)Br^+$ complex with C_{3v} point group symmetry, which is applicable to Co^{2+} centres with disordered acetate ligands in Co–CFA-1 (**3**), shows absorption bands at 5700, 9000, 10 000, 13 300, and 17 500 cm^{-1}.[20]

NMR spectroscopy

The ^{13}C CPMAS NMR spectrum of **2** is shown in Fig. 14. Five different sets of resonances with 16 different signal positions can be identified in the spectrum.

The signals around 19 ppm and 183 ppm can be assigned to the methyl ^{13}C-resonance (18.0 and 18.9 ppm, C2 and C4) and the carboxylic ^{13}C-resonance (182.0 and 183.5 ppm, C1 and C3) of the acetate ligands. From this, the presence of two different types of acetate ligands in the structure of **2** may be deduced. The remaining 12 different discernible signals are all located within the aromatic region of the spectrum (114.8,

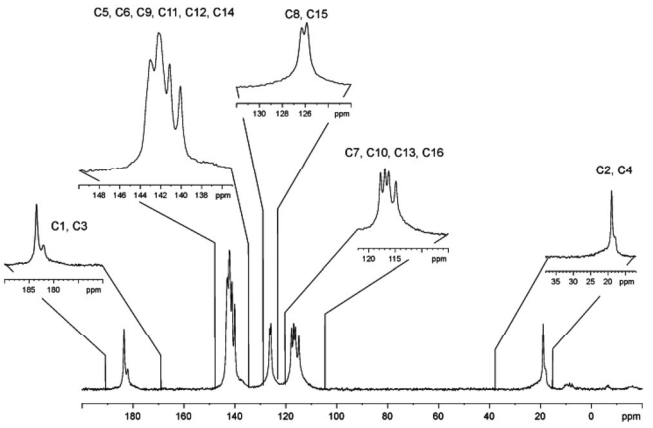

Fig. 14 ^{13}C CPMAS spectrum of CFA-1. Signal numbering according to the labelling scheme in Fig. 3.

116.2, 116.9 and 117.7 ppm; 125.8 and 125.8 ppm; 140.0, 141.1, 142.0, 142.2, 142.8, 143.0 ppm), hence confirming the existence of the two different arrangements of the bibta^{2-} ligand. An assignment of all identified signals (*cf.* Fig. S1†) is possible by a comparison of the experimental chemical shift values to the results of quantum chemical calculations as shown below. In order to obtain reasonable fits of the spectrum (DMFIT[21]), we had to incorporate a rather broad signal for each set of resonances (see ESI, Fig. S1†).

Computational studies

First-principles calculations were performed in order to study the infrared spectrum of CFA-1. Vibrational frequencies were analytically computed by determining the second derivatives of the energy with respect to the Cartesian nuclear coordinates and then transforming to mass-weighted coordinates. Given that the *P*321 unit cell contains 154 atoms ($Zn_{10}N_{36}C_{72}H_{36}$), without counting the acetate groups, the periodic system calculation of vibrational frequencies was unattainable owing to limited computing capabilities. On the other hand, with the exception of very low frequency soft modes, we expect to study with reasonable accuracy most of the infrared spectrum with the use of clusters to model CFA-1.

Gaussian09[22] was one of the software codes used throughout. DFT was used for geometry optimisations and vibrational analysis with HCTH[23] functional chosen as it gave good balanced accuracy *vs.* computational cost. The Def2-basis set[24] TZVP from Ahlrich's group was selected. Geometries of all structural models were optimised obeying full symmetry constraints.

We also employed the FHI-aims code[25] which is an all-electron electronic structure code based on numeric atom-centered orbitals. The localized basis allows for performing the calculations both for finite clusters and infinite systems employing periodic boundary conditions. For the calculations we used the GGA-PBE functional.[26] As this lacks dispersive corrections, we included them through the DFT-D scheme suggested by Tkatchenko and Scheffler.[27] The calculations were carried out with the so-called light basis set at 'tier1' level. The smallest unit cell used for geometry optimization in periodic calculations was the primitive unit cell ($a = b = 17.90$ Å, $c = 19.34$ Å, $\alpha = \beta = 90°$, $\gamma = 60°$) and the Brillouin zone was sampled in the *k*-space using the Monkhorst–Pack scheme within $1 \times 1 \times 1$ mesh points. From the periodic-DFT geometry optimisation, we subsequently extracted a cluster in order to make the vibrational analysis. Using a similar approach, Denysenko *et al.*[17] obtained vibrational frequencies in very good agreement with the experimental ones.

Small clusters may not be representative of the vibrations of the full solid with the only exception of localised vibrational modes such as for example those associated with CH and CO stretching or CH_3 bending. In order to have a realistic picture, instead of considering a representative large cluster, we have considered a set of increasingly larger clusters with the aim of comparing how different vibrations can be affected by the long-range coupling typical in an extended solid or framework.

First, the main models used were cluster-1 and cluster-2 (ESI, Fig. S2†), which contain the main secondary building unit present in CFA-1. Cluster-1 describes better the environment of an octahedral Zn atom as it contains 6 BTA (1,2,3-benzotriazolate) ligands around, whilst cluster-2 describes better the interactions between acetate ligands present in CFA-1. Two possibilities of acetate binding to the tetrahedral Zn atoms have been found: in cluster-1, the acetate ligand retains its characteristic difference between the carbonyl-type and ester-type oxygens, binding only the latter to the Zn atom, while in cluster-2 both oxygen donors of the acetate ligand are equidistant to the Zn. We will focus later on how this affects the infrared peaks observed. Secondly, a larger cluster will be proposed in order to check if the results are size-converged. All clusters are shown in the ESI.†

Finally, periodic-DFT and cluster-DFT models were set up in order to calculate the ^{13}C NMR peaks of the CFA-1 structure using the XRD data. The periodic-DFT calculations were performed with the CASTEP code[28] using the PBE functional, and a plane-waves basis set cutoff of 300 eV. Convergence thresholds were set to 0.2×10^{-5} eV per atom for the total energy. The NMR calculations were performed using the Gauge Including Projector Augmented Wave approach (GIPAW). The simulation cell consisted of the full unit cell of CFA-1 containing 210 atoms. In the cluster-DFT calculations, the HCTH functional and the Def2-TZVP basis set were employed, both for the geometry optimisation and the NMR calculation, using the largest cluster (ESI, cluster-3, Fig. S8†) in order to mimic the chemical environments of the carbon atoms as accurately as possible.

FT-IR spectra

The results of the calculated HCTH-TZVP vibrational frequencies and infrared spectra of cluster-1 and cluster-2 and the comparison with the CFA-1 experimental are available as ESI (Fig. S2 and S5†), showing that only cluster-2 reproduces the experimental spectrum. Further, an even larger cluster, containing 221 atoms, was considered in order to check if the results are size-converged. The choice of this new cluster, which we call 'cluster-3' (ESI, Fig. S8†), is based on the topology and symmetry of CFA-1 and contains structural and topological features not included in clusters 1 and 2. An overall comparison with the experimental results is shown in Fig. 15 and Table 2.

It can be seen that the calculated spectra (Fig. 15) reproduce the experimental ones quite well. Frequencies at low wave numbers (experimental 205, 256 and 277 cm^{-1} and calculated 207, 248, 261, 285 cm^{-1}) agree well and they correspond to the bending and rotating modes involving both Zn and BTA linkers. Also the peaks calculated at 1189 and 1192 cm^{-1} belong to the BTA ligand with some contribution of the Zn–BTA bonds.

The calculated frequency of 310 (320 cm^{-1} in experiments) corresponds to the acetate bending mode, with some contribution from the Zn atom.

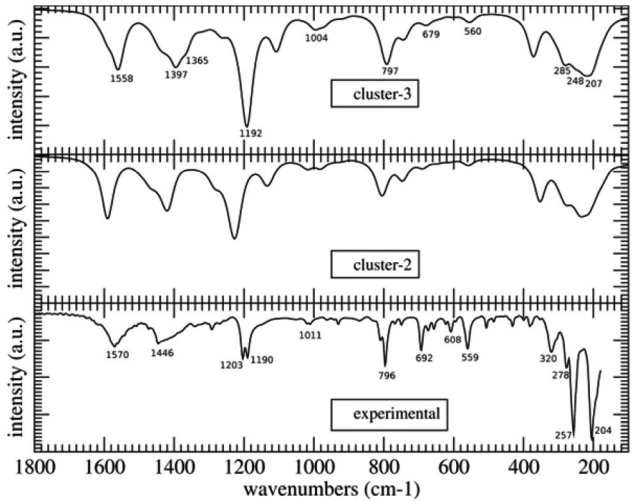

Fig. 15 GGA-PBE calculated infrared spectrum of cluster-3 (top) and HCTH/TZVP calculated infrared spectrum of cluster-2 (middle) and experimental (bottom). Clusters are shown in ESI, Fig. S4 and S8.† Assignments are given in Table 2.

Table 2 DFT calculated active normal vibrational modes in the infrared spectrum of cluster-2 (Fig. S2), cluster-3 (Fig. S8), and comparison with the experimental infrared spectrum of CFA-1. See also ESI, Fig. S5

CFA-1 (exp) (cm^{-1})	Assignment	Cluster-2 (calc) (cm^{-1})	Cluster-3 (calc) (cm^{-1})
204, 257, 278	(Zn-BTA) bending/ rotation	210–260	207, 248, 261, 285
320	Zn-acetate	295	310
559	BTA	560	560
608	Acetate	—	603
692	Acetate	689	679
796	BTA	800	797
1011	BTA	1019	1004, 1027
1190, 1203	Zn-BTA	1220–1230	1189, 1192
1446	Acetate	1414–1426	1365, 1397
1570	Acetate	1590	1558

The peaks calculated at 560, 797, 1004 and 1027 cm^{-1} belong to the BTA (1,2,3-benzotriazolate) modes and the experimental equivalents are 559, 796 and 1011 cm^{-1}.

The peaks corresponding to the acetate anions are calculated at 603, 679, 1365, 1397 and 1558 cm^{-1}, which experimentally appear at 608, 692, 1446 and 1570 cm^{-1}. The calculated value of 1365 cm^{-1} belongs to the combined CH_3 umbrella and C–C stretching mode of one acetate, and the 1397 cm^{-1} corresponds to the same mode of another acetate. The peak at 1570 cm^{-1} corresponds to the Zn–O stretching mode of one acetate ligand, and the one at 1591 cm^{-1} to the same mode of another acetate. In the experimental spectra both peaks are quite broadened, especially the one at 1446 cm^{-1}, since the acetate ligands are not completely equivalent and they are quite sensitive to the geometry and environment, much more than the other acetate vibrational modes, because they involve a stretching type of motion. Also, modes that include CH_3 umbrella motion of the acetate ligand start at around 1320 cm^{-1}. More details are given as ESI.†

The experimentally observed frequencies at 1190 and 1203 cm^{-1} belong to the BTA ligand mode. Similar to some of the acetate modes, these two modes belong to the same stretching mode but for the two different BTA types (see ESI, Fig. S6 and S7†). Since there is the same amount of the two linkers in the structure, they are expected to have peaks with the same intensities, and since differences are small, the positions of the two peaks are close to each other. In the calculated spectra, peaks are at 1189 and 1192 cm^{-1}. Due to the less constraints and symmetry in the cluster, the two modes do not have the same intensity; they have closer values and in the broadened spectra, where they appear as one peak.

As expected, two BTAs and especially two types of acetate ligands give two different values for the vibrational stretching modes. Vibrational modes that involve ligand bending or slight rotation are mostly the same for the two ligand types (modes below 900 cm^{-1}). Also, values of the experimental and calculated frequencies overlap quite well. Only larger differences are for the broadened peak at 1446 cm^{-1}. This is not a surprise because the same stretching mode calculated for the cluster is reduced approximately by 30 cm^{-1} compared to the periodic case. Other modes are not sensitive to the type of calculation, either being cluster- or periodic-type.

^{13}C NMR calculated spectrum of CFA-1

Results of cluster- and periodic-DFT calculations of the ^{13}C chemical shifts are indicated in Table 3, where a comparison with the experimental results is provided.

First, it can be seen that, overall, cluster-DFT are more accurate than periodic-DFT results, and this is due to two factors. On the one hand, the large size of cluster-3 has allowed to reproduce accurately the local carbon-environment which influences the chemical shifts. On the other hand, the fact

Table 3 ^{13}C NMR chemical shifts (ppm) of CFA-1 as calculated and from experiment

Carbon label[a]	Periodic-DFT calculated[b]	Cluster-DFT calculated	Experimental
C1 (6)	164.3	181.6, 184.3	179.6, 182.0, 183.5
C3 (2)	164.3	180.2	
C2 (6)	23.2	19.9, 21.1	18.0, 18.9, 21.7
C4 (2)	22.8	21.2	
C5 (6)	152.4	141.4	140.0, 142.0, 142.2, 142.8
C6 (6)	151.2	141.0	
C11 (6)	150.9	141.2	
C12 (6)	152.1	141.5	
C7 (6)	124.9	117.0	114.8, 116.2, 116.9, 117.7
C10 (6)	126.2	116.0	
C13 (6)	123.6	116.3	
C16 (6)	125.4	116.7	
C8 (6)	135.3	128.2	125.8, 126.3
C15 (6)	135.5	128.2	
C9 (6)	151.9	141.1	141.0, 143.3
C14 (6)	149.8	143.0	

[a] See Fig. 3. The number of atoms in the unit cell in parentheses. [b] For all equivalent carbons (except C1–C4) all values are similar. Values are averaged. Carbons C1–C4 are discussed in a different section.

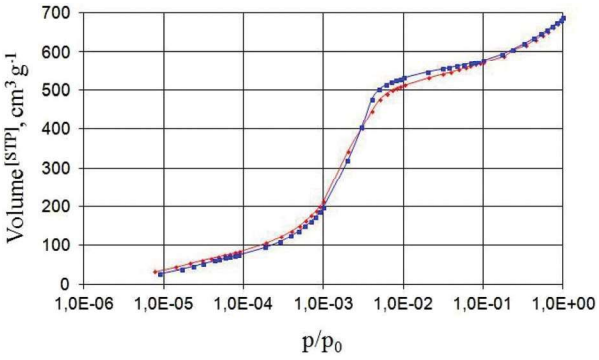

Fig. 16 Representative argon adsorption isotherms at 77 K on a semilogarithmic scale for a desolvated samples of **2** (red) and **3** (blue).

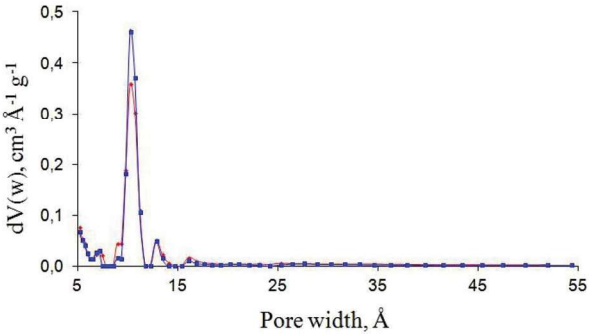

Fig. 17 Pore size distributions for **2** (red) and **3** (blue) calculated by fitting NLDFT models to the argon adsorption data.

that the cluster is a smaller system has allowed to employ a more accurate methodology. In particular, the chemical shifts are sensitive to the quality of the basis set and the basis set employed in the cluster (Def2-TZVP) is clearly outperforming the plane wave cutoff of 300 eV employed in the periodic calculation. A comparison of the cluster-DFT NMR results with experiment shows excellent agreement (Table 3). A graphic comparison of the experimental and calculated results (ESI, Fig. S10†) shows an average absolute difference below 2 ppm, which can be considered very accurate.[29]

Gas sorption measurements

Both compounds, **2** and **3**, exhibit permanent porosity, which was confirmed by argon gas sorption. Adsorption isotherms obtained with Ar gas at 77 K are very similar for both samples and reveal a type-I sorption behaviour, which is characteristic of microporous solids (Fig. 16). Pore volumes obtained from the sorption isotherms by using an NLDFT method are 0.756 $cm^3\ g^{-1}$ for **2** and 0.762 $cm^3\ g^{-1}$ for **3**. These values are close to the values expected from the crystallographic data (0.784 $cm^3\ g^{-1}$ for the solvent free crystal and 1.68 Å probe radius, calculated by using PLATON/SQUEEZE[12] program), indicating that the pore structure remains stable upon solvent removal. Fitting the adsorption data to the BET equation gives as well nearly the same surface area values of 1965 $m^2\ g^{-1}$ for **2** and 2003 $m^2\ g^{-1}$ for **3**.

To evaluate the pore size distribution of both compounds, the argon sorption isotherms sampled at 77 K were analysed using non-local density functional theory (NLDFT)[30] implementing a carbon equilibrium transition kernel for argon adsorption at 77 K based on a slit-pore model.[31] The distributions calculated by fitting the adsorption data (Fig. 17) reveal the pores mainly in the range of 9–12 Å with a maximum located at 10.3 Å, reflecting an average pore width calculated from crystallographic data (6.18–14.35 Å).

Conclusion

In conclusion, we have synthesised and structurally characterized a chiral metal–organic framework (CFA-1) containing Kuratowski-type pentanuclear coordination units. Exchanging peripheral zinc atoms of these units by redox-active metal centres, a host of functional microporous networks should thus become available. The fact that the ligand is synthesised within a single reaction step, starting from an inexpensive commercial precursor, should render this novel material particularly attractive for applications requiring large quantities (*e.g.* in separation or adsorption applications). Employing chiral solvents (or co-ligands, respectively) in the synthesis of CFA-1 should lead to homochiral samples of CFA-1 samples, which could then be employed in asymmetric (catalytic) reactions. These efforts will require (laboratory) analytical characterisation techniques in order to evaluate the relative ratio of both enantiomorphous crystal forms obtained from the reaction. However, at present, appropriate chiral detection methods devoted to insoluble crystalline samples are considerably less developed in comparison to the well-established approaches frequently applied in the production and analysis of chiral molecular compounds (*i.e.* (V)CD spectroscopy, or NMR spectroscopy employing chiral shift reagents), and they will require major adaptations.

Experimental section

Materials and methods

All starting materials were of reagent grade and used as received from the commercial supplier. Thermogravimetric analysis (TGA) was performed with a TGA Q500 analyser in the temperature range of 25–800 °C in flowing nitrogen at a heating rate of 10 K min^{-1}. Argon gas sorption isotherms were measured with a Quantachrome Autosorb-I ASI-CP-8 instrument. Prior to measurements, the samples were heated at 250 °C for 20 h in high vacuum to remove occluded solvent molecules. Argon sorption experiments were performed at 77 K in the range of $1.0 \times 10^{-5} \leq P/P_0 \leq 0.99$ with argon gas. Fourier transform infrared (FT-IR) spectra were recorded with ATR in the range 4000–180 cm^{-1} on a Bruker Equinox 55 FT-IR spectrometer. Diffuse reflectance UV/Vis/NIR spectra were recorded in the range 2000–250 nm on a Perkin Elmer λ 750 s spectrometer. Energy-dispersive X-Ray spectroscopy (EDX) was

performed with a Philips XL 30 scanning electron microscope. Solid-state CPMAS NMR experiments were performed employing a 7 T Bruker Avance III solid state NMR spectrometer operating at resonance frequencies of 75.4 MHz and 300.13 MHz for ^{13}C and ^{1}H, respectively. Magic Angle Spinning (MAS) NMR experiments were performed using a Bruker 4 mm WVT MAS probe at spinning speeds of 10 000 Hz, using cross polarization (CP) techniques and high power TPPM[32] decoupling to detect the ^{13}C signal. 4096 scans were accumulated with a repetition delay of 5 s and the spectrum was referenced relative to the ^{13}C signal of TMS.

Synthesis of 1*H*,1′*H*-5,5′-bibenzo[*d*][1,2,3]triazole (1)

The achiral H_2-bibta ligand was synthesised in one step from commercially available 3,3′,4,4′-tetraaminobiphenyl. To a cooled suspension of 3,3′,4,4′-tetraaminobiphenyl (1 g, 4.67 mmol) in CH_3COOH (13 mL) and H_2O (1 mL), $NaNO_2$ (0.71 g, 10.23 mmol) in 1.1 mL H_2O was added dropwise under good stirring, maintaining a temperature of 0 °C. The formed precipitate was filtered off and washed with H_2O and MeOH.

Yield: 1.05 g (95%). Mp = 342.6 °C; ^{1}H NMR (400 MHz, DMSO, δ (ppm)): 15.83 (s, 2H, NH), 8.24 (s, 2H, ArH), 8.02 (d, J = 8 Hz, 2H, ArH), 7.84 (d, J = 8 Hz, 2H, ArH). ^{13}C NMR (100 MHz, DMSO, δ (ppm)): 145.20, 139.20, 136.50, 130.10, 127.90, 127.40. IR (ν (cm^{-1})): 3070.53, 2982.48, 2894.79, 2763.99, 1512.90, 1414.05, 1248.85, 1198.44, 1024.59, 861.15, 796.40, 546.01, 422.26. Elemental analysis calcd (%): C 61.01, H 3.41, N 35.58; found: C 61.24, H 3.20, N 35.30.

Synthesis of $[Zn_5(OAc)_4(bibta)_3]$ (2)

A mixture of zinc acetate dihydrate (37.17 mg, 0.17 mmol) and H_2-bibta (10 mg, 0.04 mmol) was dissolved in 4 mL *N*-methylformamide (NMF) and the solution was placed in a glass tube (10 mL). The tube was sealed and heated at 90 °C for 3 days and then cooled to room temperature. The precipitate was filtered, washed with NMF (3 × 1 mL) and MeOH (3 × 3 mL) and dried at 250 °C under vacuum.

Yield: 51 mg (89%). IR (ν (cm^{-1})): 2982.48, 2763.99, 1632.82, 1414.05, 1271.94, 1248.85, 1198.44, 1024.59, 796.40, 546.01, 422.26. Elemental analysis calcd (%): C 41.75, H 2.39, N 19.92; found: C 40.85, H 2.20, N 19.56.

General procedure for Co/Zn exchange in $[Zn_5(OAc)_4(bibta)_3]$ (2)

CFA-1 (10 mg, 0.008 mmol) was heated with the solution of cobalt(II) acetate tetrahydrate in NMF (4 mL, concentration range: 0.001 mol L^{-1}–0.300 mol L^{-1}) for 24 h at 60 °C. The violet precipitate was filtered off, washed first with hot NMF, until the filtrate was completely colourless, and subsequently with MeOH (3 × 3 mL), after which it was dried at 250 °C in vacuum. The Co/Zn molar ratio of the product was determined by energy-dispersive X-Ray spectroscopy (EDX).

Synthesis of $[Zn(CoZn_3)(OAc)_4(bibta)_3]$ (3)

Cobalt(II) acetate tetrahydrate (3.0 mg, 0.012 mmol) was dissolved in NMF (4 mL) and CFA-1 (10 mg, 0.008 mmol) was added to the solution. The reaction mixture was stirred for 24 h at 60 °C. The violet precipitate was filtered off and washed with NMF (3 × 1 mL) and MeOH (3 × 3 mL) and dried at 250 °C in vacuum. Elemental analysis calcd (%): C 41.96, H 2.40, N 20.02; found: C 41.85, H 2.42, N 19.86.

Single-crystal X-ray crystallography

The crystal was transferred to Paratone-N oil and mounted on a CryoLoop (both Hampton Research Corp.). The data were collected at 100 K using synchrotron radiation on beamline BL14.2 of the Joint Berlin-MX Laboratory at BESSY-II (Berlin, Germany) with a MX-225 CCD detector (Rayonics, Illinois). The data were integrated and scaled with the XDS software package.[33] The structure was solved using direct methods with the help of SHELXS-97[34] and refined by full-matrix least squares techniques using SHELXL-97. Non-hydrogen atoms were refined with anisotropic temperature parameters. The hydrogen atoms were positioned geometrically and refined using a riding model (Table 4).

Powder X-ray diffraction measurements and crystal structure determination of Co–CFA-1, $[Zn(CoZn_3)(OAc)_4(bibta)_3]$ (3)

Crystalline samples were ground using an agate mortar and pestle, and were deposited in the hollow of a zero-background sample holder. Diffraction data were collected in the 2θ range of 4–90° with 0.02° steps, with an interval of 6 s per step, using a Seifert XRD 3003 TT diffractometer equipped with a Meteor 1D detector. For the thermal stability characterization, the samples were ground using an agate mortar and pestle and were loaded into a glass capillary (Hilgenberg, diameter 0.5 mm). The variable temperature XRPD experiment data were collected in the 2θ range of 4–60° with 0.02° steps, with an interval of 0.5 s per step using a Bruker A8 Advance

Table 4 Crystal data and structure refinement for **2**

Empirical formula	$C_{44}H_{30}N_{18}O_8Zn_5$
Formula weight	1265.71
Temperature	100(2) K
Wavelength	0.88561 Å
Crystal system, space group, no.	Trigonal, *P*321, no. 150
Unit cell dimensions	a = 17.750(3) Å c = 19.192(4) Å
Volume	5236.7(15) $Å^3$
Z, calculated density	2, 0.803 g cm^{-3}
Absorption coefficient	2.097 mm^{-1}
F(000)	1268
Crystal size	0.06 × 0.04 × 0.04 mm
Theta range for data collection	1.65° to 33.98°
Limiting indices	$-22 \le h \le 21$, $-22 \le k \le 22$, $-24 \le l \le 10$
Reflections collected/unique	17 630/7177 [R(int) = 0.0556]
Completeness to theta = 33.98	97.4%
Absorption correction	None
Refinement method	Full-matrix least-squares on F^2
Data/restraints/parameters	7177/7/257
Goodness-of-fit on F^2	1.044
Final R indices [$I > 2\sigma(I)$]	R_1 = 0.0450
R indices (all data)	wR_2 = 0.1131
Absolute structure parameter	0.033(9)
Largest diff. peak and hole	1.041 and −0.426 e A^{-3}

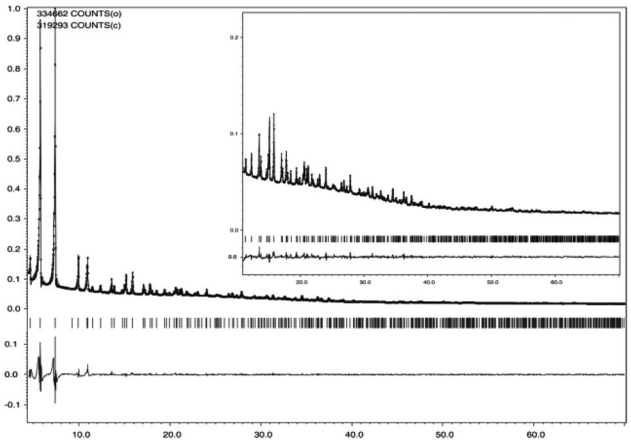

Fig. 18 The Rietveld refinement plots for **3**. Dotted and solid lines represent observed and calculated patterns, respectively, with peak markers and the difference plot shown at the bottom. For clarity, the insert shows an expanded view in the range of 11–70° 2θ.

diffractometer equipped with a Lynxeye linear position-sensitive detector, an MRI TCPU1 oven, in transmission geometry. The samples were heated from room temperature to 50, 150, 250, 350, and 400 °C, and once the corresponding temperature was reached, the sample was kept at this temperature for 10 min before starting to measure. For compound **3**, a Rietveld refinement process was directly carried out starting from the structural model of **2** from the single crystal data. The sample was heated for 24 h at 250 °C in vacuum to remove the solvent molecules. Many attempts were made to refine the structure based on a measurement from the flat specimen. Unfortunately, the refinement process was unstable; *R*-values were in the range of 18–22%. A strong preferred orientation in the [001] direction was detected. For Rietveld refinement we used a long measurement in a capillary (4–70° 2θ, 0.02°, 8 s per step), collected in transmission geometry. The Rietveld refinement was carried out using Jana2006 program.[35] Weak geometric restraints on bond distances were used during the refinement. Hydrogen atoms were placed at idealized positions using SHELXL program. The final Rietveld refinement plots for **3** are presented in Fig. 18. The crystal data and structure refinement summary for $[Zn(CoZn_3)(OAc)_4(bibta)_3]$ are presented in ESI, Table S4.† Atom coordinates and selected distances and angles are presented in ESI, Tables S5–S7.†

Complete crystallographic data for the structures **2**, CFA-1 and **3**, Co–CFA-1 reported in this paper have been deposited in the CIF format with the Cambridge Crystallographic Data Center as supplementary publication no. CCDC 930634 and 930635.

Acknowledgements

Financial support by the DFG (Priority Program SPP 1362 "Porous Metal–organic Frameworks") is gratefully acknowledged. G. Sastre thanks the Spanish government for the provision of the programme "Severo Ochoa" (project SEV 2012 0267), and SGAI-CSIC for computing time. The authors are grateful to Dr U. Mueller for support during single crystals measurements and the Helmholtz Centre, Berlin for financing the travel costs to BESSY II. The authors are grateful to J. Jelic (Dept. of Chemistry, TU Munich) for performing DFT calculations on CFA-1 structure models employing periodic boundary conditions.

Notes and references

1 (*a*) O. M. Yaghi, H. Li, C. Davis, D. Richardson and T. L. Groy, *Acc. Chem. Res.*, 1998, **31**, 474; (*b*) M. Eddaoudi, D. B. Moler, H. Li, B. Chen, T. M. Reineke, M. O'Keeffe and O. M. Yaghi, *Acc. Chem. Res.*, 2001, **34**, 319; (*c*) S. Kitagawa, R. Kitaura and S.-I. Noro, *Angew. Chem., Int. Ed.*, 2004, **43**, 2334; (*d*) S. L. James, *Chem. Soc. Rev.*, 2003, **32**, 276.

2 (*a*) G. Feréy, *Chem. Soc. Rev.*, 2008, **37**, 191; (*b*) A. U. Czaja, N. Trukhan and U. Müller, *Chem. Soc. Rev.*, 2009, **38**, 1284; (*c*) L. Ma, C. Abney and W. Lin, *Chem. Soc. Rev.*, 2009, **38**, 1248; (*d*) D. Farrusseng, S. Aguado and C. Pinel, *Angew. Chem., Int. Ed.*, 2009, **41**, 7638; (*e*) J. Kuppler, J. Timmons, Q.-R. Fang, J.-R. Li, A. Makal, D. Young, D. Yuan, D. Zhao, W. Zhuang and H.-C. Zhou, *Coord. Chem. Rev.*, 2009, **253**, 3042.

3 J. S. Seo, D. Whang, H. Lee, S. I. Jun, J. Oh, Y. J. Jeon and K. Kim, *Nature*, 2000, **404**, 982.

4 (*a*) O. R. Evans, H. L. Ngo and W. J. Lin, *J. Am. Chem. Soc.*, 2001, **123**, 10395; (*b*) W. J. Lin, *Solid State Chem.*, 2005, **178**, 2486; (*c*) C.-D. Wu, A. Hu, L. Zhang and W. J. Lin, *J. Am. Chem. Soc.*, 2005, **127**, 8940; (*d*) L. Ma and W. J. Lin, *J. Am. Chem. Soc.*, 2008, **130**, 13834.

5 (*a*) C. J. Kepert, T. J. Prior and M. J. Rosseinsky, *J. Am. Chem. Soc.*, 2000, **122**, 5158; (*b*) D. Bradshaw, T. J. Prior, E. J. Cussen, J. B. Claridge and M. J. Rosseinsky, *J. Am. Chem. Soc.*, 2004, **126**, 6106.

6 (*a*) T. Ezuhara, K. Endo and Y. Aoyama, *J. Am. Chem. Soc.*, 1999, **121**, 3279; (*b*) L. Ma, C. Abney and W. Lin, *Chem. Soc. Rev.*, 2009, **38**, 1248–1256.

7 T. Ezuhara, K. Endo and Y. Aoyama, *J. Am. Chem. Soc.*, 1999, **121**, 3279.

8 (*a*) S. Biswas, M. Tonigold and D. Volkmer, *Z. Anorg. Allg. Chem.*, 2008, **634**, 2532; (*b*) S. Biswas, M. Tonigold, M. Speldrich, P. Kögerler, M. Weil and D. Volkmer, *Inorg. Chem.*, 2010, **49**, 7424; (*c*) Y.-Y. Liu, M. Grzywa, M. Tonigold, G. Sastre, T. Schüttrigkeit, N. S. Leeson and D. Volkmer, *Dalton Trans.*, 2011, **40**, 5926; (*d*) D. Denysenko, M. Grzywa, M. Tonigold, B. Streppel, I. Krkljus, M. Hirscher, E. Mugnaioli, U. Kolb, J. Hanss and D. Volkmer, *Chem.–Eur. J.*, 2011, **17**, 1837.

9 (*a*) J. H. Marshall, *Inorg. Chem.*, 1978, **17**, 3711; (*b*) V. L. Himes, A. D. Mighell and A. R. Siedle, *J. Am. Chem. Soc.*, 1981, **103**, 211; (*c*) G. F. Kokoszka, J. Baranowski, C. Goldstein, J. Orsini, A. D. Mighell, V. L. Himes and A. R. Siedle, *J. Am. Chem. Soc.*, 1983, **105**, 5627;

(*d*) J. Handley, D. Collison, C. D. Garner, M. Helliwell, R. Docherty, J. R. Lawson and P. A. Tasker, *Angew. Chem., Int. Ed*, 1993, **32**, 1036; (*e*) E. G. Bakalbassis, E. Diamantopoulou, S. P. Perlepes, C. P. Raptopoulou, V. Tangoulis, A. Terzis and T. F. Zafiropoulos, *J. Chem. Soc., Chem. Commun.*, 1995, 1347; (*f*) V. Tangoulis, C. P. Raptopoulou, A. Terzis, E. G. Bakalbassis, E. Diamantopoulou and S. P. Perlepes, *Inorg. Chem.*, 1998, **37**, 3142; (*g*) M. Murrie, D. Collison, C. D. Garner, M. Helliwell, P. A. Tasker and S. S. Turner, *Polyhedron*, 1998, **17**, 3031; (*h*) V. Tangoulis, C. P. Raptopoulou, A. Terzis, E. G. Bakalbassis, E. Diamantopoulou and S. P. Perlepes, *Mol. Cryst. Liq. Cryst.*, 1999, **335**, 463; (*i*) W. Jinling, Y. Ming, Y. Yun, Z. Shuming and M. Fangming, *Chin. Sci. Bull.*, 2002, **47**, 890; (*j*) Y.-X. Yuan, P.-J. Wei, W. Qin, Y. Zhang, J.-L. Yao and R.-A. Gu, *Eur. J. Inorg. Chem.*, 2007, 4980.

10 S. Biswas, M. Grzywa, H. P. Nayek, S. Dehnen, I. Senkovska, S. Kaskel and D. Volkmer, *Dalton Trans.*, 2009, 6487–6495.

11 (*a*) W. Kaminsky, *J. Appl. Crystallogr.*, 2005, **38**, 3; (*b*) W. Kaminsky, *J. Appl. Crystallogr.*, 2007, **40**, 2.

12 A. L. Spek, *J. Appl. Crystallogr.*, 2003, **36**, 7.

13 *Quantachrome Autosorb, Version 1.56*, 2009.

14 VESTA V3.1: K. Momma and F. Izumi, *J. Appl. Crystallogr.*, 2011, **44**, 1272–1276.

15 QuteMol V0.4.1: M. Tarini, P. Cignoni and C. Montani, *IEEE Trans. Vis. Comput. Graphics*, 2006, **12**(5), 1237–1244.

16 V. A. Blatov and D. M. Proserpio, *TOPOS – program package for multipurpose crystallochemical analysis, Version 4.0*.

17 D. Denysenko, T. Werner, M. Grzywa, A. Puls, V. Hagen, G. Eickerling, J. Jelic, K. Reuter and Dirk Volkmer, *Chem. Commun.*, 2012, **48**, 1236–1238.

18 *OriginPro 8.5.0.G*, OriginLab Corporation, 2010.

19 A. B. P. Lever in *Inorganic Electronic Spectroscopy*, 1984, p. 492.

20 (*a*) I. Bertini, M. Ciampolini and L. Sacconi, *J. Coord. Chem.*, 1973, **1**, 73; (*b*) I. Bertini, D. Gatteschi and A. Scozzafava, *Inorg. Chem.*, 1975, **14**, 812.

21 D. Massiot, F. Fayon, M. Capron, I. King, S. Le Calvé, B. Alonso, J.-O. Durand, B. Bujoli, Z. Gan and G. Hoatson, *Magn. Reson. Chem.*, 2002, **40**, 70.

22 M. J. Frisch, G. W. Trucks, H. B. Schlegel, G. E. Scuseria, M. A. Robb, J. R. Cheeseman, G. Scalmani, V. Barone, B. Mennucci, G. A. Petersson, H. Nakatsuji, M. Caricato, X. Li, H. P. Hratchian, A. F. Izmaylov, J. Bloino, G. Zheng, J. L. Sonnenberg, M. Hada, M. Ehara, K. Toyota, R. Fukuda, J. Hasegawa, M. Ishida, T. Nakajima, Y. Honda, O. Kitao, H. Nakai, T. Vreven, J. A. Montgomery, Jr., J. E. Peralta, F. Ogliaro, M. Bearpark, J. J. Heyd, E. Brothers, K. N. Kudin, V. N. Staroverov, R. Kobayashi, J. Normand, K. Raghavachari, A. Rendell, J. C. Burant, S. S. Iyengar, J. Tomasi, M. Cossi, N. Rega, J. M. Millam, M. Klene, J. E. Knox, J. B. Cross, V. Bakken, C. Adamo, J. Jaramillo, R. Gomperts, R. E. Stratmann, O. Yazyev, A. J. Austin, R. Cammi, C. Pomelli, J. W. Ochterski, R. L. Martin, K. Morokuma, V. G. Zakrzewski, G. A. Voth, P. Salvador, J. J. Dannenberg, S. Dapprich, A. D. Daniels, Ö. Farkas, J. B. Foresman, J. V. Ortiz, J. Cioslowski and D. J. Fox, *GAUSSIAN 09 (Revision A.1*), Gaussian, Inc., Wallingford, CT, 2009.

23 A. D. Boese and N. C. Handy, *J. Chem. Phys.*, 2001, **114**, 5497–5503.

24 (*a*) F. Weigend and R. Ahlrichs, *Phys. Chem. Chem. Phys.*, 2005, **7**, 3297–3305; (*b*) A. Schaefer, C. Huber and R. Ahlrichs, *J. Chem. Phys.*, 1994, **100**, 5829–5835; (*c*) K. Eichkorn, F. Weigend, O. Treutler and R. Ahlrichs, *Theor. Chem. Acc.*, 1997, **97**, 119–124; (*d*) F. Weigend, F. Furche and R. Ahlrichs, *J. Chem. Phys.*, 2003, **119**, 12753–12762; (*e*) D. Andrae, U. Haeussermann, M. Dolg, H. Stoll and H. Preuss, *Theor. Chim. Acta*, 1990, **77**, 123–141.

25 V. Blum, R. Gehrke, F. Hanke, P. Havu, V. Havu, X. Ren, K. Reuter and M. Scheffler, *Comput. Phys. Commun.*, 2009, **180**, 2175–2196.

26 J. P. Perdew, K. Burke and M. Ernzerhof, *Phys. Rev. Lett.*, 1996, **77**, 3865–3868.

27 A. Tkatchenko and M. Scheffler, *Phys. Rev. Lett.*, 2009, **102**, 073005.

28 (*a*) S. J. Clark, M. D. Segall, C. J. Pickard, P. J. Hasnip, M. J. Probert, K. Refson and M. C. Payne, *Z. Kristallogr.*, 2005, **220**(5–6), 567–570; (*b*) J. R. Yates, C. J. Pickard and F. Mauri, *Phys. Rev. B: Condens. Matter*, 2007, **76**, 024401.

29 V. Barone, O. Crescenzi and R. Improta, *Quant. Struct.–Act. Relat.*, 2002, **21**, 105–118.

30 P. I. Ravikovitch and A. V. Neimark, *Colloids Surf.*, 2001, **187**, 11.

31 J. Jagiello and M. Thommes, *Carbon*, 2004, **42**, 1227.

32 A. E. Bennet, C M. Rienstra, M. Auger, K. V. Lakshmi and R. G. Griffin, *J. Chem. Phys.*, 1995, **103**, 6951.

33 W. Kabsch, *J. Appl. Crystallogr.*, 1988, **21**, 67.

34 G. Sheldrick, *Acta Crystallogr., Sect. A: Fundam. Crystallogr.*, 2008, **64**, 112.

35 V. Petricek, M. Dusek and L. Palatinus, *The Crystall. Computing System*, 2006.